Materials Science in Semiconductor Processing 168 (2023) 107847

Contents lists available at ScienceDirect

Materials Science in Semiconductor Processing

journal homepage: www.elsevier.com/locate/mssp

Decoration of MoO_{3-x} on clay mineral matrix with great phosphorescence properties for oxygen activation, photochemical properties, bactericidal and oxidase-like mimics for prompt detection of pesticide

Khursheed Muzammil [a], Muhaned Zaid [b], Uday Abdul-Reda Hussein [c], Maryam Hazem Abduljabbar [d], Sarah Salah Jalal [e], Mazin A.A. Najm [f], Mohammad Y. Alshahrani [g], Abbas F. Almulla [h,i,j], Ali Alsaalamy [k], Ramadan Fallah Amer [l,m], Baadal Jushi Janani [m,*]

[a] Department of Public Health, College of Applied Medical Sciences, Khamis Mushait Campus, King Khalid University, Abha, 62561, Saudi Arabia
[b] Department of Pharmacy, Al-Manara College for Medical Sciences, (Maysan), Iraq
[c] College of Pharmacy, University of Al-Ameed, Iraq
[d] Department of Pharmacy, Al-Noor University College, Nineveh, Iraq
[e] College of Pharmacy, National University of Science and Technology, Dhi Qar, Iraq
[f] Pharmaceutical Chemistry Department, College of Pharmacy, Al-Ayen University, Thi-Qar, Iraq
[g] Department of Clinical Laboratory Sciences, College of Applied Medical Sciences, King Khalid University, Abha, Saudi Arabia
[h] College of Technical Engineering, The Islamic University, Najaf, Iraq
[i] College of Technical Engineering, The Islamic University of Al Diwaniyah, Iraq
[j] College of Technical Engineering, The Islamic University of Babylon, Iraq
[k] College of Technical Engineering, Imam Ja'afar Al-Sadiq University, Al-Muthanna, 66002, Iraq
[l] Nanobiotechnology Laboratory, Institute of Technology, Chennai, India
[m] Department of Chemistry, Academy of Materials Science, Navi Mumbai, India

ARTICLE INFO

Keywords:
Singlet oxygen
Hallyosite
MoO_{3-x}
Photochemical
Antibacterial
Peroxidase

ABSTRACT

In photocatalytic system, singlet oxygen can be generated based on the excitonic energy transfer process. Here, the 2D layered hallyosite (Hal) as a support hydroxyl group's substrate to anchor molybdenum trioxide (MoO_{3-x}) with oxygen vacancies (Hal/MoO_{3-x}) was prepared. Electron spin resonance and quenching experiments showed that the combination of Hal and MoO_{3-x} enhances the generation of singlet oxygen ($^1O_2$) and inhibits the production of other reactive oxygen species. Furthermore, photocatalytic molecular oxygen activation experiments were carried out to evaluation of $^1O_2$ generation. Phosphorescence spectroscopy revealed improved triplet exciton production in the composite. The Hal/MoO_{3-x} shows great degradation response in TC removal. The value for the rate constant (k) of the composite was 0.0209 min^{-1} under light irradiation, which is about 5.64 and 3.02 times larger than that of Hal, MoO_3 and MoO_{3-x}, respectively. The results revealed that Hal/MoO_{3-x} had the best antibacterial performance. The L. *monocytogenes*, and *N. gonorrhoeae* were killed by the destruction of the cell membranes due to the generation of reactive oxygen species and thermal effect. In addition, a colorimetric sensor via the Hal/MoO_{3-x} and peroxidase system was performed for selectivity and sensitivity detection of simazine with 2.45 nM as a detection limit.

1. Introduction

Singlet oxygen is a reactive oxygen species and utilized in green synthesis, photodynamic cancer therapy and wastewater purification, due to high reactivity and oxidize ability [1–3]. The $^1O_2$ shows stronger degrading selectivity to environmental intervention than hydroxyl radicals [4]. The conventional view of photo-generated carriers suggests that it may be generated by the oxidation process for the superoxide radical ($\bullet O_2^- + h^+ \rightarrow {}^1O_2$) [5]. However, the $^1O_2$ was producted by the photocatalyst conduction band potential is higher than the generation of

* Corresponding author. Department of Chemistry, Academy of Materials Science, Navi Mumbai, India.
E-mail address: bajujanani@gmail.com (B.J. Janani).

https://doi.org/10.1016/j.mssp.2023.107847
Received 15 June 2023; Received in revised form 3 September 2023; Accepted 12 September 2023
Available online 20 September 2023
1369-8001/

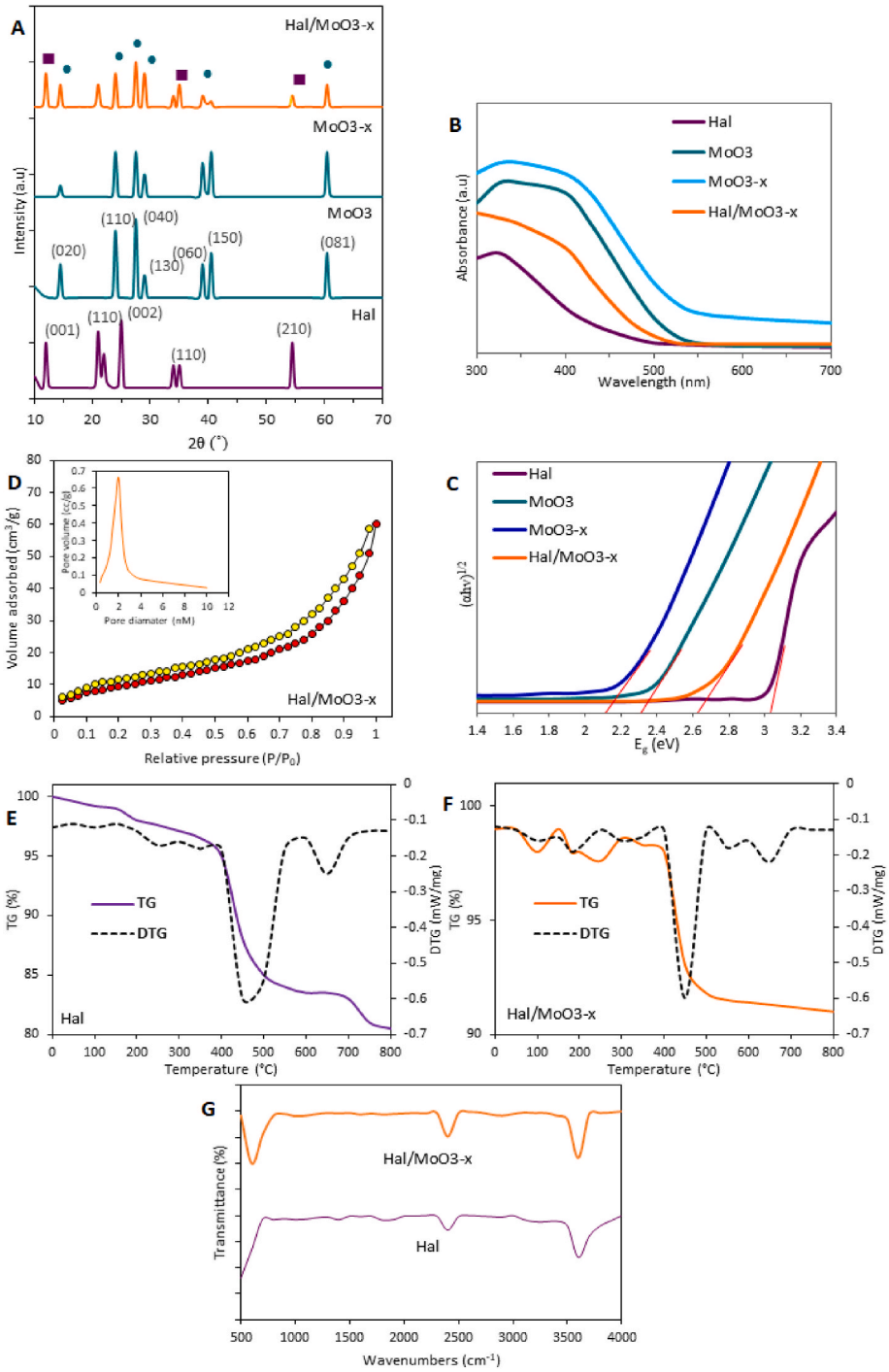

Fig. 1. XRD curve (A), UV–vis spectra (B), Kubelka-Munk (C), BET plot (D), TGA/DTG spectra (E, F), and FTIR spectrum (G) of the prepared materials.

$\bullet O_2^-$ potential [6,7]. In general, coulomb interaction between electrons and holes, singlet excitons are formed. Through effective singlet to triplet inter-system crossing, the triplet exciton of the photosensitizer will be formed and can transfer energy to $^3O_2$, producing $^1O_2$ [8]. This means, during $^3O_2$ activation, the generation of $^1O_2$ is mainly due to resonant energy transfer between the triplet exciton in the catalyst [9].

The previous studies showed that the efficiency of light-driven oxygen activation, a conversion process depends on the energy coupling between photons, excitons and the catalyst [10–13]. The previous study shows nanomaterials were activated under other reactive oxygen species such as hydroxyl radical, and super dioxide radicals [14–16].

Among them, as an oxygen-deficient semiconductor such as molybdenum trioxide with oxygen vacancy (MoO_{3-x}) has received a great deal of interest [17]. For instance, Morita et al. found that WO_{3-x} nanoparticles had distinctive light-absorption capabilities [18]. Also, the natural clay minerals make an excellent choice as catalyst carriers due to their high adsorption turnover, chemical stability, affordability, recycling, and bioavailability [19,20]. Hallyosite (Hal) is a representative clay mineral with a layered structure, is commonly utilized in environmental treatment as a catalyst support substrate [21]. The higher specific surface area make the contact reaction between pollutants and catalysts and improving the catalytic response. Moreover, the hydroxyl groups of Hal play a major role in the catalytic process. This condition can enhance the mass transfer rate of O_2 and pollutant molecules on the

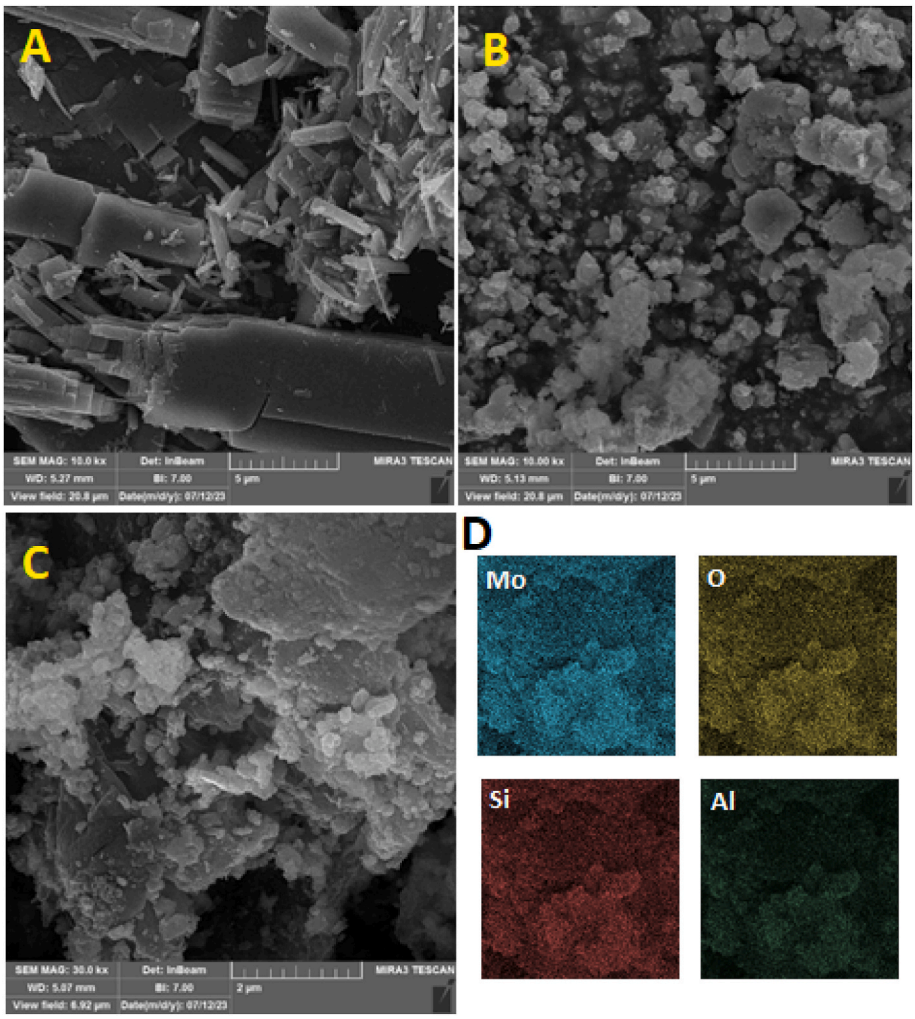

Fig. 2. FESEM images of Hal (A), MoO_{3-x} (B), Hal/MoO_{3-x} (C), mapping images (D) of Hal/MoO_{3-x}.

catalytic process [21].

Simazine is the most pesticide was applied in numerous industries in the word, and is very harmful contaminant of ground water [22]. The release of simazine pesticide in the ground water causes several human diseases [23]. Moreover, simazine makes males health problems such as reduced spermatogenesis, and fertility [23–26]. Therefore, different ways to evaluate of pesticide in aquatic water, but these methods is not complete to finding. Therefore colorimetric detection via peroxidase activity in the previous studies showed the best method to detection of pollution in aquatic water [27–29].

Therefore, this study hallyosite was used as a substrate to anchor MoO_{3-x} and prepared hallyosite/MoO_{3-x} nanocomposites. The Hal loading the MoO_{3-x} nanoparticles exhibited great efficiently to producing $^1O_2$. The morphology, and structural of hallyosite/WO_{3-x} composites were investigated. The phosphorescence spectroscopy shows that hallyosite/MoO_{3-x} nanocomposites have higher triplet exciton concentrations, can be the generation of $^1O_2$. Results showed that the higher $^1O_2$ production of hallyosite/MoO_{3-x} compared to the raw material. This study investigated the ability of photocatalysis to antibacterial activities. The peroxidase-like catalytic activity of hallyosite/MoO_{3-x} was tested by the oxidation of TMB in presence of H_2O_2. This way is utilized for the colorimetric detection of simazine in an aqueous medium.

2. Experimental

2.1. Materials

Materials and reagents are provided in Support Information Text S1.

2.2. Preparation of hallyosite/MoO_{3-x} sample

MoO_3 nanosheets were prepared by hydrothermal method. Firstly, 5.0 mL of concentrated HNO_3 was dropped into a beaker containing 25 mL of deionized water, and the HNO_3 solution was formed after thorough stirring. Then, 1.5 mmol of ammonium molybdate was dissolved in 10 mL of deionized water to form a clear solution, and then added to the above HNO_3 solution. After stirring vigorously for 30 min, it was reacted at 180 °C for 3.0 h in Teflon autoclave. After cooling to room temperature, the produced precipitate was collected by centrifugation and washed with deionized water and anhydrous ethanol three times, and finally dried in an oven at 60 °C for 12 h.

The MoO_{3-x} prepared by the above hydrothermal method was mixed well with $NaBH_4$ in a mortar at a certain mass ratio and then transferred to a quartz boat. Then the quartz boat was calcined in a tube furnace at 350 °C under N_2 atmosphere for 640 min. After the sample was cooled to room temperature, the sample was placed in a beaker containing 100 mL of deionized water and washed with stirring for 24 h. Finally, the sample was collected by centrifugation and washed three times with deionized water, three times with anhydrous ethanol, and dried at 60 °C for 12 h.

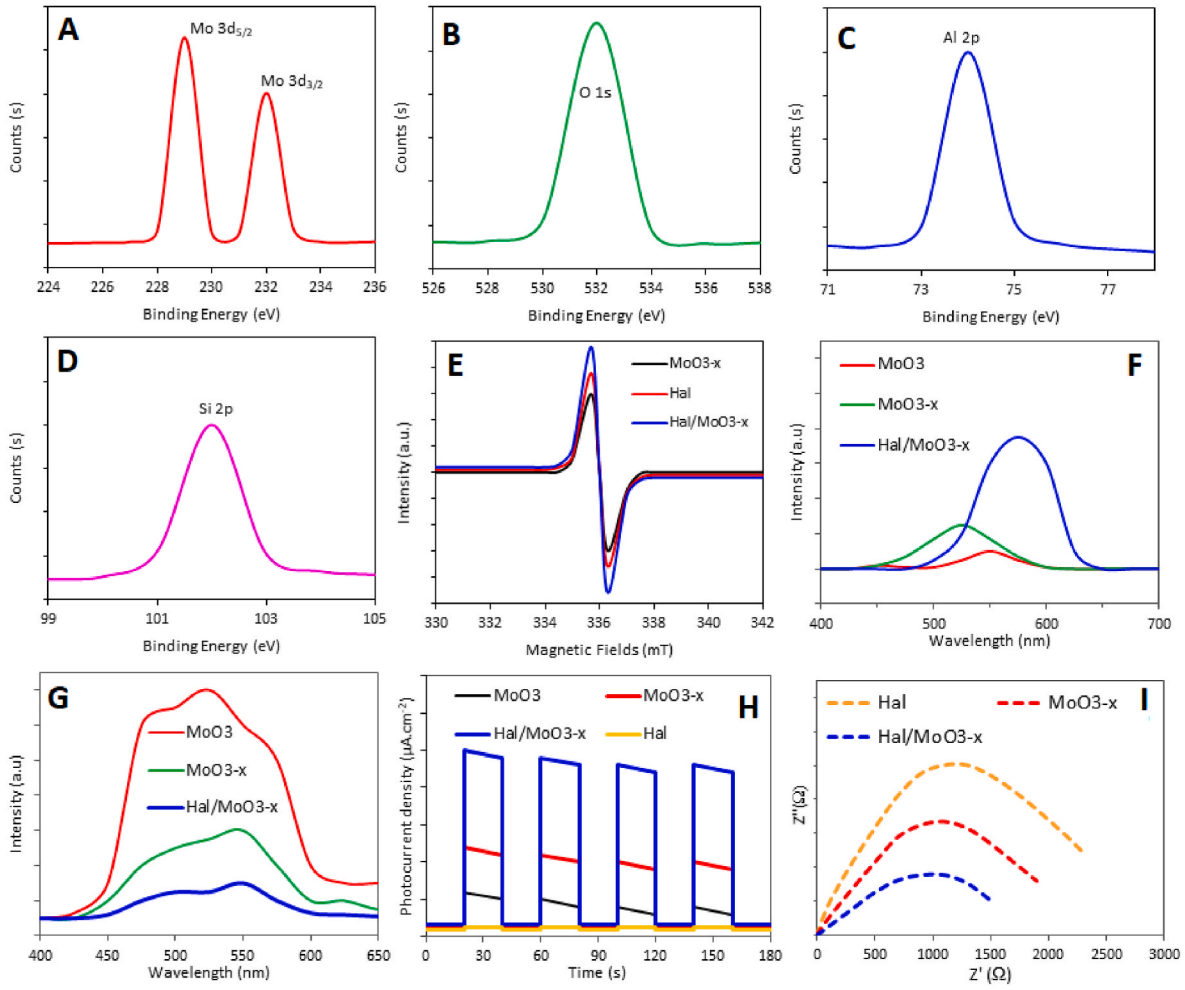

Fig. 3. XPS survey spectrum, (A) Mo 3d, (B) O 1s, (C) Al 2p (D) Si 2p for Hal/MoO_{3-x}, ESR spectra (E), Phosphorescence (PH) spectra (F), photoluminescence spectra (G), Photocurrents density curve (H), and EIS plot (I) of samples.

The Hal/MoO_{3-x} sample were prepared using the above method. Firstly, the amount of MoO_3 and Hal was 0.2 g and the 0.4 g of $NaBH_4$ was mix the above ingredients in the mortar with the determined mass ratio, and then transferred to the quartz boat. Then the quartz boat was calcined in a tube furnace at 350 °C under N_2 atmosphere for 640 min. After the sample was cooled to room temperature, the sample was placed in a beaker containing 100 mL of deionized water and washed with stirring for 24 h. Finally, the sample was collected by centrifugation and washed three times with deionized water, three times with anhydrous ethanol, and dried at 60 °C for 12 h.

2.3. Reactive oxygen species evaluation

The electron spin resonance test were conducted using an electron spin resonance spectrometer (Billerica, MA) at 27 °C. The experimental light source was a 300 W xenon lamp without a filter. 5 μL of control or sample solutions were put in capillary tubes and inserted into the ESR cavity. In the detection of different reactive oxygen species, 25 mM DMPO was used as spin trap for hydroxyl radicals, 2 mM 4-oxo-TEMP was chosen for detection of singlet oxygen, 25 mM BMPO was used to detect superoxide radical [30,31].

2.4. Catalytic tests of TC degradation

The photocatalytic performance was investigated by degradation of tetracycline (TC). Firstly, 20 mL of 20 mg/L TC solution was measured and then 20 mg of the prepared catalyst was dispersed in TC solution and stirred continuously. After 40 min of dark reaction to reach the equilibrium, then the photocatalytic reaction was started by turning on the 300 W xenon lamp [32–34]. The residual concentration of TC was measured by a UV–Vis spectrophotometer at 358 nm. To investigate the effect of reactive oxygen species on degradation of TC, $^1O_2$, $O_2^{\bullet-}$, and •OH were trapped using the trapping agents NaN_3 (0.1 M), Anthraquinone (0.1 M), and Isopropyl alcohol (0.1 M), respectively.

2.5. Characterization

The relevant data regarding testing equipment was shown in Text S2.

2.6. Antibacterial test

The agar diffusion method can be studied to test the antibacterial potential of the synthesized Hal/MoO_{3-x} nanocomposites. *Listeria monocytogenes* and *Neisseria gonorrhoeae* were used as gram$^+$, and gram$^-$ bacterial, respectively. The culture of the test organism was added to the nutrient agar medium before placed into a Petri dish. The plate medium was allowed to harden at 27 °C [35,36]. The cups were placed in each plate and were spaced equally apart. Two bacteria were suspended in sterile water and diluted to 10^8 CFU/mL. At concentrations of 10, 25, 50, and 100 mg/L were created. The 50 μL of each concentration was added to the cups. The petri dishes were incubated for 24 h at 37 °C. Then, the zones of inhibition was measured.

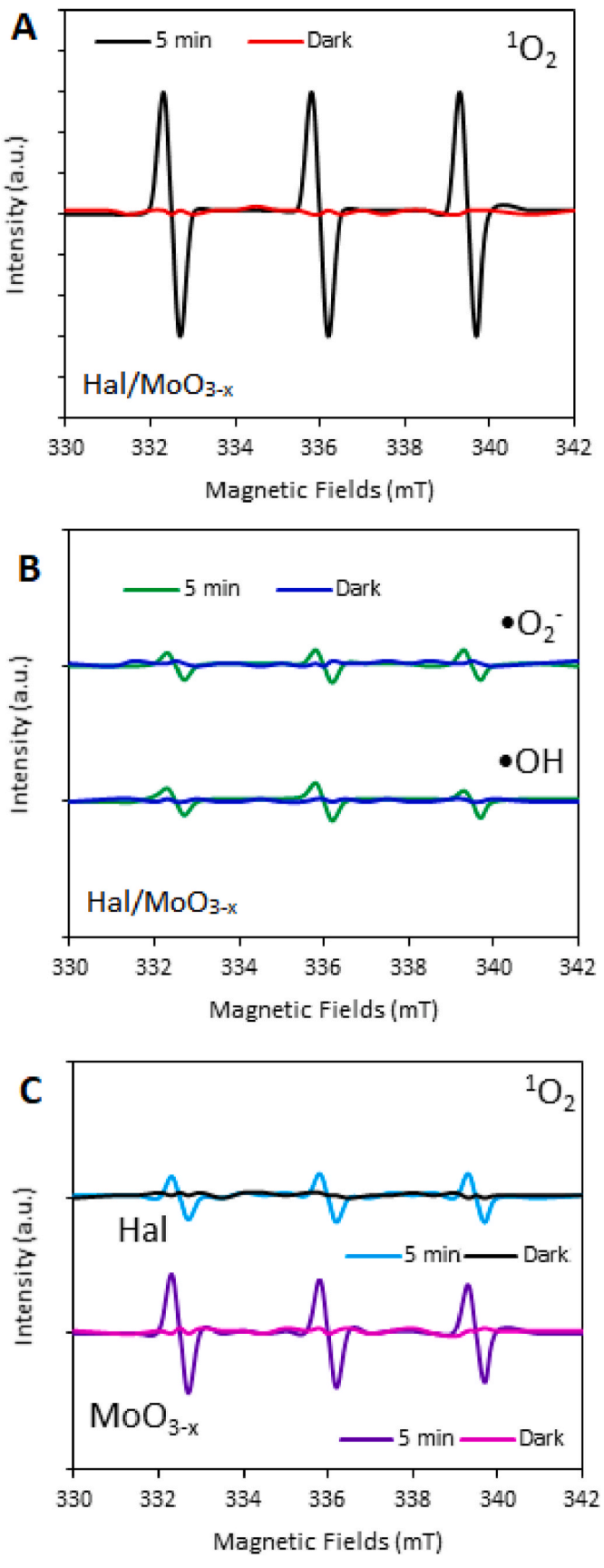

Fig. 4. ESR spectra of different samples under TEMP-$^1O_2$, DMPO-•O_2^-, and DMPO-•OH adducts under dark and 5min irradiation.

2.7. Colorimetric detection of simazine

The synthesized Hal/MoO_{3-x} nanocomposites were sonicated to disperse in deionized water. The peroxidase-like activity was examined *via* the oxidation of TMB (20 μM) by H_2O_2 (1 mM) in HAc-NaAc buffer. The absorption spectra were monitored at 652 nm by a spectrophotometer. To detection of simazine by Hal/MoO_{3-x} nanocomposites as a probe, 30 μL of simazine solutions and 2 mg/L of Hal/MoO_{3-x} nanocomposites were dispersed in the buffer solution. After thought, the suspension were incubated at 27 °C and different concentrations of simazine were added. For selectivity evaluation, interfering species as various metal ions, and proteins were added into the reactor. The status of simazine in the sensing systems were analyzed by the UV–vis spectrophotometer. The practical applicability of the prepared sensor was experimented by adding simazine and Hal/MoO_{3-x} nanocomposites to water samples such as tap water, and river water. The recovery was evaluated by standard method.

3. Results and discussion

3.1. Morphological and structural studies

The crystal phase of the samples were reported by XRD. Fig. 1A shows peaks at 2θ = 12.21°, 21.03°, 25.51°, 35.12°, and 55.24° from the hallyosite (Hal) with peak patterns as (001), (110), (002), (110), and (210) crystal planes, respectively (JCPDS# 29–1487) [21]. The diffraction peaks of the MoO_3 and MoO_{3-x} appear at 14.23° (020), 24.12° (110), 27.36° (040), 29.10° (130), 39.18° (060), 41.16° (150) and 59.94° (081), from the orthorhombic phase of MoO_3 crystal (JCPDS# 35–0609) [37]. The diffraction peaks intensity of MoO_{3-x} was weaker than peaks of MoO_3, confirming a lower crystallinity. Two-phase structure belonging to Hal and MoO_{3-x} was observed for Hal/MoO_{3-x} nanocomposites.

The optical properties of the prepared materials was reported by UV–Vis absorption spectroscopy and demonstrated in Fig. 1B. As can be seen, Hal has light absorption only in the UV region, and the absorption band edge of MoO_3 is located at about 500 nm [38]. The spectra of MoO_{3-x} shows the light absorption is red-shifted and absorption is enhanced, which shows the defect states from the generation of oxygen vacancies in band structures [39–41]. Moreover, the spectra of Hal/-MoO_{3-x} shows the wide light absorption range due to the loading of MoO_{3-x}. The absorbance band gap was estimated from the Kubelka-Munk equation [42]. The plot of $(\alpha h\nu)^{1/n}$ vs. $h\nu$ is used to distinguish the optical energy gap. The band gap energies of Hal, MoO_3, MoO_{3-x} and Hal/MoO_{3-x} are calculated and shown in Fig. 1C. The band gap energies of Hal, MoO_3, MoO_{3-x} and Hal/MoO_{3-x} are 3.03 eV, 2.31 eV, 2.14 eV, and, 2.62 eV, respectively. The red shift of MoO_{3-x} due to bandgap narrowing and atom-packing defects present in the nanoparticles [43]. In Hal/MoO_{3-x}, the native defects MoO_{3-x} from oxygen vacancies causes the decreases band gap of Hal.

To investigate the surface adsorption properties of Hal/MoO_{3-x}, BET tests were carried out [44,45]. The adsorption-desorption isotherm plot were shown in Fig. 1D. The isotherms demonstrate the materials with mesoporous properties. According to the results, the Hal/MoO_{3-x} composites exhibits specific surface area and average pore size were 52.34 m^2/g and 2.12 nm, respectively (Table S1). The TGA, DTG and FT-IR spectra of Hal and Hal/MoO_{3-x} are shown in Fig. 1E, and F. The TGA spectrum of Hal shows the thermal decomposition process can be divided into three stages. The first stage is due to the removal of physically adsorbed water at to 300 °C. The second stage is due to convert and, the surface aluminum hydroxyl group (Al–OH) bond breaks at 300 °C–700 °C. The third stage is due to dihydroxylation process during degradation of halloysite at 700 °C [46]. Similarly, the TGA spectrum of Hal/MoO_{3-x} shows the thermal decomposition remains consistent, confirming the great thermal stability of MoO_{3-x}. The FT-IR spectra of Hal shows the peak for the Al–OH (located at 3600-3700 cm^{-1}) [47]. The

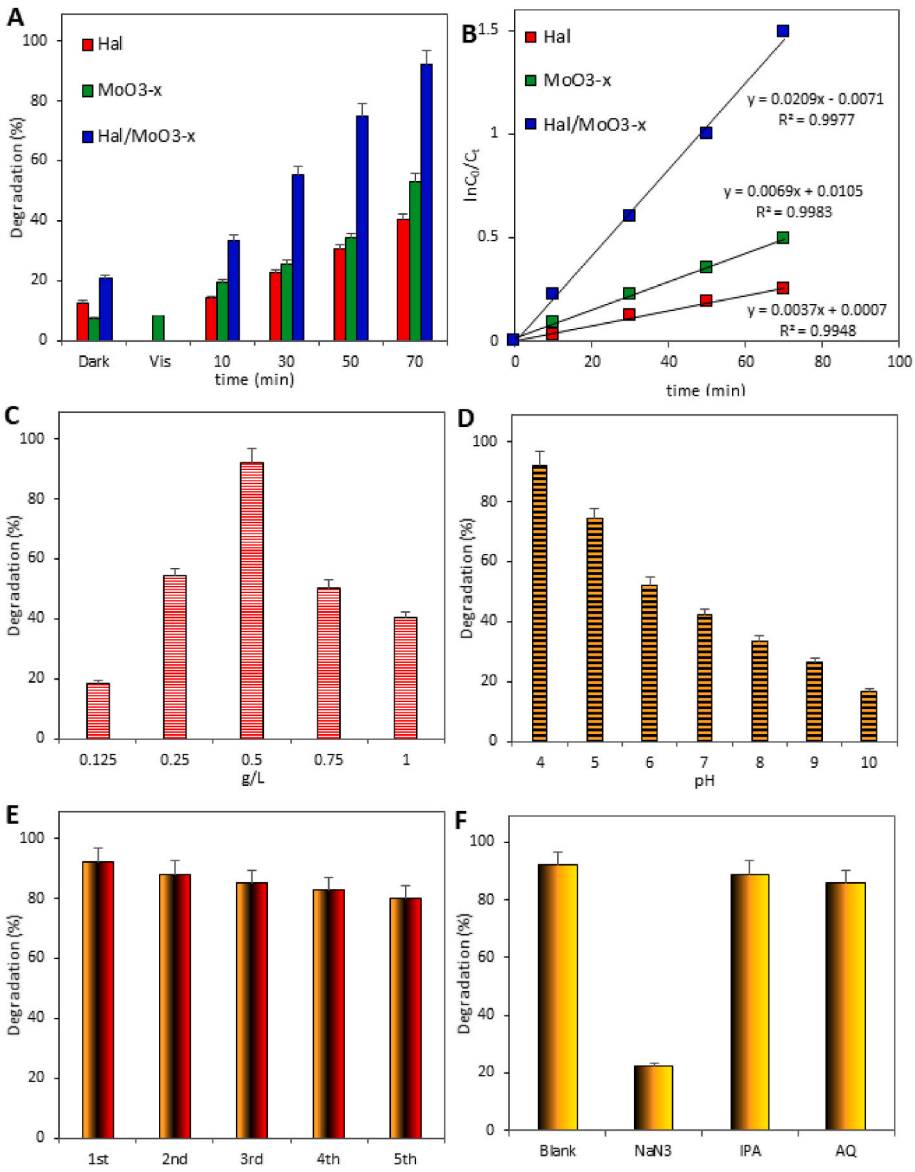

Fig. 5. Photo-degradation of TC by different catalysts under visible light irradiation (A), kinetic plot of degradation system (B), effect of Hal/MoO_{3-x} catalyst dosage (C), effect of pH on TC degradation (D), recyclability test (E), and quenching test (F) of Hal/MoO_{3-x} for degradation of TC.

FT-IR spectra of Hal/MoO_{3-x} shows the peak at 3600-3700 cm^{-1} due to Al–OH, and also, the Mo–O peak at 600 cm^{-1}, due to the presence of MoO_{3-x} in nanocomposites [37].

Fig. 2A displays the FESEM image of the Hal shows that the surface is roughened, but still retains the typical lamellar structure of halloysite. The FESEM image of prepared MoO_{3-x} (Fig. 2B) with the crystal surface becomes rough. From Fig. 2C, the MoO_{3-x} nanoparticles are uniformly dispersed on the lamellar Hal. In addition, as depicted in Fig. 2D from mapping images, Mo and O elements are uniformly distributed on the surface of Hal, which can also prove that the MoO_{3-x} nanoparticles are successfully loaded on the Hal surface.

Using the XPS method, the surface elemental valence states of the Hal/MoO_{3-x} were analyzed by the XPS survey spectrum and are illustrated in Fig. 3. The high-resolution Mo 3d XPS spectrum (Fig. 3A) was two peaks at 229.6 and 231.61 eV respectively due to a spin-orbit splitting of $Mo3d_{5/2}$ and $Mo3d_{3/2}$, respectively [37]. The O 1s spectrum of Hal/MoO_{3-x} composite is displayed in Fig. 3B. It can be seen that the O 1s XPS spectra shows the one peak at 531.3 eV can be ascribed to the generation of oxygen vacancies (O_V) [37]. The high resolution XPS spectra of the Al 2p (Fig. 3C) and Si 2p (Fig. 3D) showed the characteristic binding energies at 74.90 eV and 102.90 eV, respectively [21].

For the purpose of direct disclosure of the existence of oxygen vacancies, electron spin-resonance spectroscopy (ESR) was conducted [18]. Fig. 3E shows the ESR signal of unpaired e^- trapped in the surface oxygen vacancies. Compared to Hal and MoO_{3-x}, the higher intensity of the Hal/MoO_{3-x} composite, confirms the higher concentration of oxygen vacancies in the composites [19].

The phosphorescence (PH) and photoluminescence (PL) experiments were performed to investigate the excitonic effects on the photo-excitation process. As displayed in Fig. 3F, the observation of the phosphorescence emission confirms the presence of a triplet exciton in the Hal/MoO_{3-x} system. In addition, the phosphorescence intensity of the Hal/MoO_{3-x} sample differs significantly from that of MoO_3 and MoO_{3-x}, indicating that the Hal/MoO_{3-x} sample has a significantly higher concentration of triplet excitons, which would be advantageous for $^1O_2$ generation through the energy transfer process [48,49].

The PL spectra were recorded to identify the generated e^-/h^+ pair separation. Fig. 3G, where the pristine MoO_3 shows the highest PL intensity under the excitation wavelength due to the severe recombination

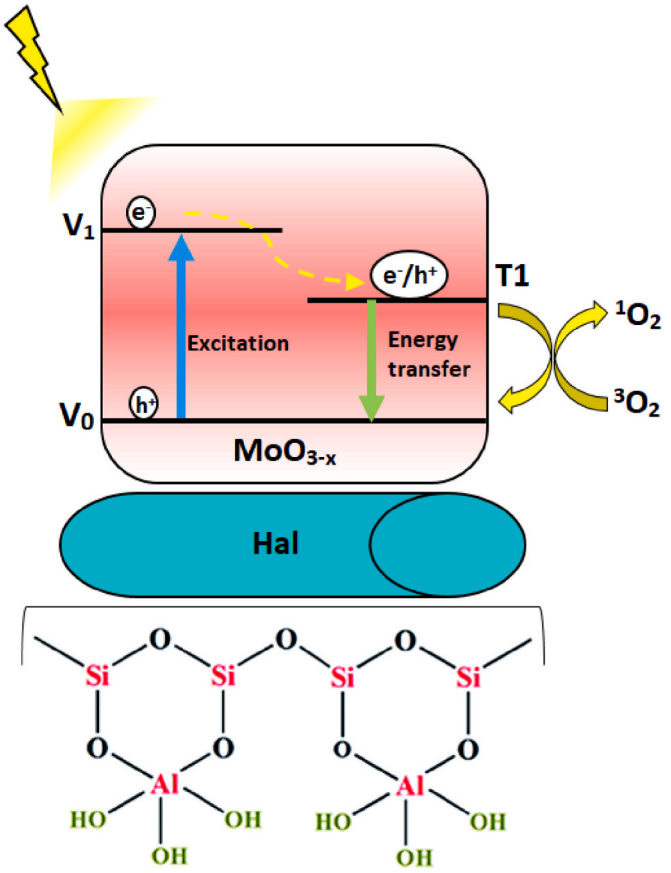

Fig. 6. Proposed mechanism for Hal/MoO_{3-x} in photocatalytic system.

of generated carriers [50]. The PL spectra of the MoO_{3-x}, Hal/MoO_{3-x} samples are similar, both with a significant decrease in PL emission intensity [50]. The PL quenching of Hal/MoO_{3-x} is obvious with loading MoO_{3-x} on the Hal surface, due to the Hal enhances the energy level transfer of generated electrons in MoO_{3-x}, which that implying that the charge transfer was more effective, and improvements of exciton energy transfer [50].

Fig. 3H shows the photocurrent density curves of the prepared nanocomposites [27]. The curves show that Hal/MoO_{3-x} has a relatively higher photocurrent density, which is due to the strong exciton effect resulting in less hot electron generation by the catalyst. The Hal/MoO_{3-x} behaves at the greatest intensity, suggesting excellent charge carrier separation ability. The prepared MoO_3 and MoO_{3-x} exhibit lower photocurrent densities, which indicates their weaker photo-response. In addition, the enhanced photocurrent density of MoO_{3-x} compared to MoO_3 is due to the introduction of oxygen vacancies, and inhibition of generated e^-/h^+ recombination. The lower photocurrent of Hal is due to the low light absorption and the high resistance [51].

Electrochemical impedance spectroscopy (EIS) were reported to the conductivity of the samples (Fig. 3I). The EIS spectra of Hal/MoO_{3-x} is slightly smaller compared to Hal, indicating a lower internal resistance, which is attributed to the loading of MoO_{3-x}. Although there are some differences in conductivity with the Hal and Hal/MoO_{3-x}, they both have very high internal resistance, which is due to the properties of the clay minerals [51].

3.2. Reactive oxygen species testing

The oxygen activation was detected by utilizing the Hal/MoO_{3-x} as probe. The ROS produced by Hal/MoO_{3-x} in dark condition and light irradiation were studied by ESR test. The presence of TEMP-$^1O_2$ adducts (Fig. 4A), DMPO-$O_2^{\bullet-}$ adducts and DMPO-•OH adducts (Fig. 4B) were detected [52]. As shown in Fig. 4, there was no ROS signals in the dark condition, but reactive oxygen species ($^1O_2$, $O_2^{\bullet-}$ and •OH) were checked for light irradiation condition. Notably, the intensity of the signal peak of the Hal/MoO_{3-x} composite was significantly strong, which indicated a higher concentration of $^1O_2$ and confirmed the high activity of the catalyst during the light irradiation. This will represent a stronger degradation and a higher selective oxidation for the contaminants by the Hal/MoO_{3-x} composite. Interestingly, the extremely high $^1O_2$ production (with no production of other ROS) indicated the existence of other mechanisms in the Hal/MoO_{3-x} photocatalytic system that differ from the conventional e^- and h^+ production. Therefore, a mechanism of the $^1O_2$ production based on the excitonic effect was considered to explain this phenomenon [52]. Moreover, the reactive oxygen species ($^1O_2$) was checked for Hal, and MoO_{3-x} materials. The results showed that the peak of the Hal, and MoO_{3-x} are weaker than Hal/MoO_{3-x} (Fig. 4C). This will represent a stronger degradation and highly selective oxidation for the contaminants by the Hal/MoO_{3-x}.

3.3. Photocatalysis performances

The Hal/MoO_{3-x} with producing $^1O_2$ is projected to be a promising photocatalyst for selective oxidation processes. So, the photocatalytic activity of different samples was assessed by degradation of tetracycline (TC). As shown in Fig. 5A, the Hal/MoO_{3-x} had the highest photocatalytic activity under light irradiation with the degradation rate of 92.0%, while the Hal, and MoO_{3-x} had lower degradation rates. The higher photocatalytic activity of Hal/MoO_{3-x} may be benefited due to the large specific surface area. Moreover, the improvement of defect content is important to increase the responsiveness of the photocatalyst, however, the presence of large number of defects will become a combination center of generated e^- and h^+. MoO_{3-x} had the lowest contaminant removal rates in the presence and absence of light, which could be attributed to the rapid e^-/h^+ recombination [53–55]. The pseudo-first-order rate constants [27] for TC degradation were displayed in Fig. 5B. The value for the rate constant (k) of the Hal/MoO_{3-x} was 0.0209 min^{-1} under light irradiation, which is about 5.64 and 3.02 times larger than that of Hal (0.0037 min^{-1}), and MoO_{3-x} (0.0069 min^{-1}), respectively.

Experiments were conducted to investigate the effects of catalyst dose on degradation of TC in the presence of Hal/MoO_{3-x}. The enhancement of TC degradation was found when the Hal/MoO_{3-x} dose was raised from 0.125 to 0.5 g/L, as illustrated in Fig. 5C. However, no additional improvement in degradation performance was seen when the Hal/MoO_{3-x} dose was raised from 0.5 to 1.0 g/L. This might be owing to the extra catalyst scavenging the ROS, as well as the fact that increased turbidity lowers light penetration in water [56].

The TC decomposition over Hal/MoO_{3-x} composite in different pH solutions was displayed in Fig. 5D. The final degradation effect was nearly indistinguishable in the pH = 4–10 range [56]. With the increase of pH value to 10, the degradation rate of TC was increased faster, which may be attributed to the small amount of hydroxyl radical production under alkaline conditions.

The cycling test is shown in Fig. 5E, where the TC degradation performance of Hal/MoO_{3-x} decreased from 92% to 80% after the fifth cycle times. This result is mainly triggered by the surface of the catalyst was slowly inactivated after several times [57]. In addition, the XRD of the used Hal/MoO_{3-x} after 5th cycles showed a stable diffraction peak with no change in its position and compared to the XRD of the fresh Hal/-MoO_{3-x}, which that shows the structural stability of the photocatalyst (Fig. S1). The quenching test were applied to confirm the main reactive species for degradation of TC by Hal/MoO_{3-x} system. NaN_3, IPA and AQ were used as $^1O_2$, •OH, and $\bullet O_2^-$ scavengers, respectively. As shown in Fig. 5F, in the absence of the quencher, TC degraded about 92.0% in 70 min. However, the addition of NaN_3 to a decrease of TC degradation efficiency to 22.1%. While, AQ and IPA had almost no inhibitory

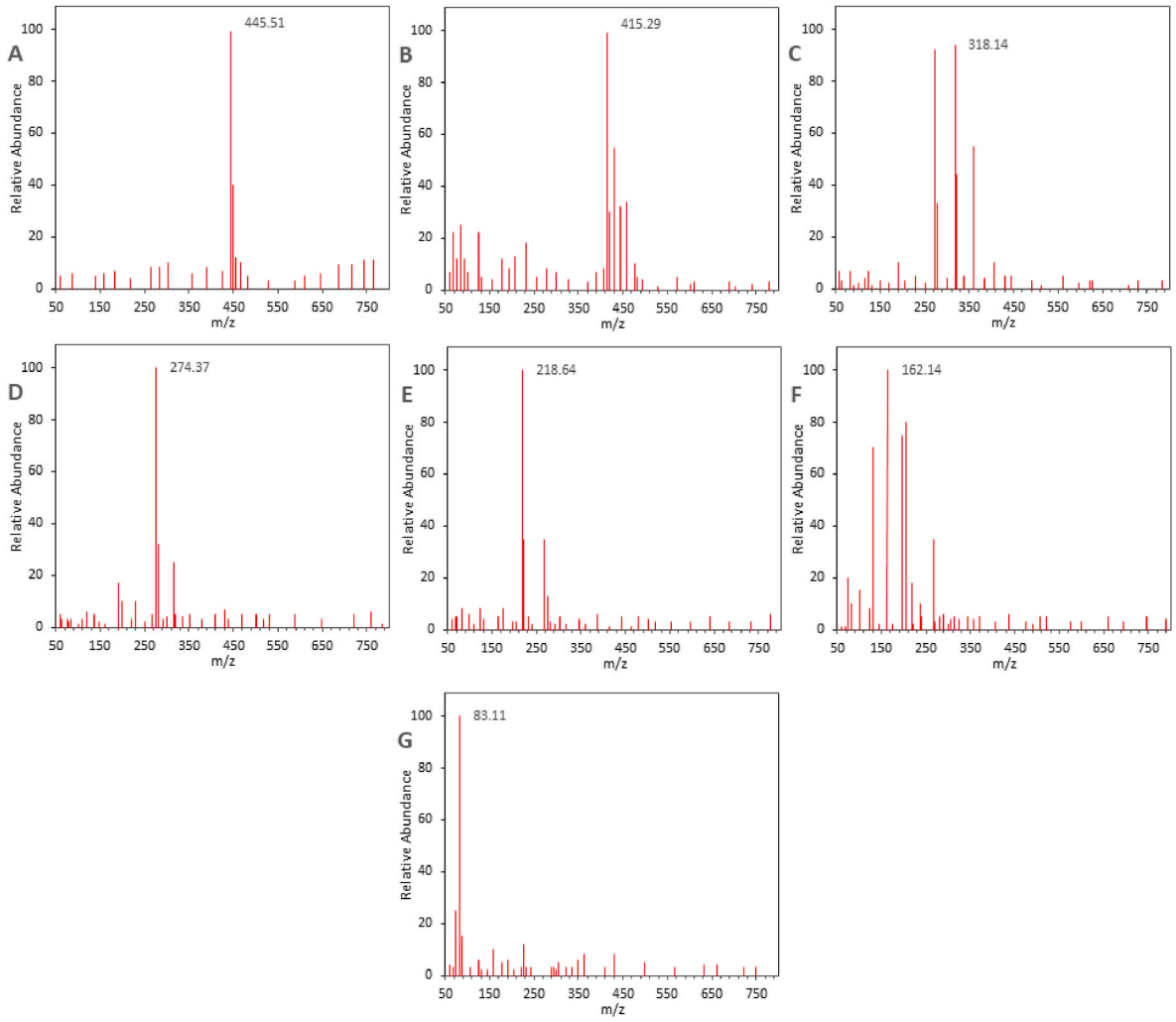

Fig. 7. LC-EIS-MS spectrum of TC (A) and transformation products (B–G).

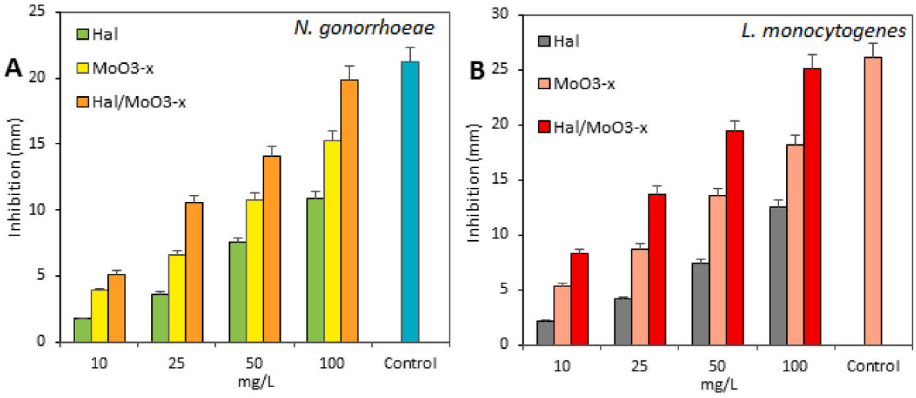

Fig. 8. The inhibition zone values of antibacterial ability of different materials.

influence on TC degradation by using the Hal/MoO_{3-x} system. This result confirms that $^1O_2$ is the dominant ROS in the degradation of TC by using the Hal/MoO_{3-x} nanocomposites.

The mechanism of the Hal/MoO_{3-x} photocatalytic system can involve an energy transfer process between the excited triplet exciton and the $^3O_2$ to produce $^1O_2$ (Fig. 6). As can be seen, under irradiation, electrons of Hal and MoO_{3-x} in the ground state (V_0) are excited into the singlet state (V_1) and holes are generated in the ground state V_0. The singlet exciton can be formed due to interaction between e^- and h^+. Then, the resonance energy transfer process between the triplet exciton in the catalyst and the $^3O_2$, which then excites the $^3O_2$ to form $^1O_2$. The $^1O_2$ can be degraded TC under irradiation [4].

The intermediates from degradation of TC were detected by liquid chromatography/Electrospray Ionisation/mass spectrometry (LC-ESI-MS) [58,59] (Fig. 7) and a resulted analysis of the degradation system for the ability of Hal/MoO_{3-x} was performed. The transformation

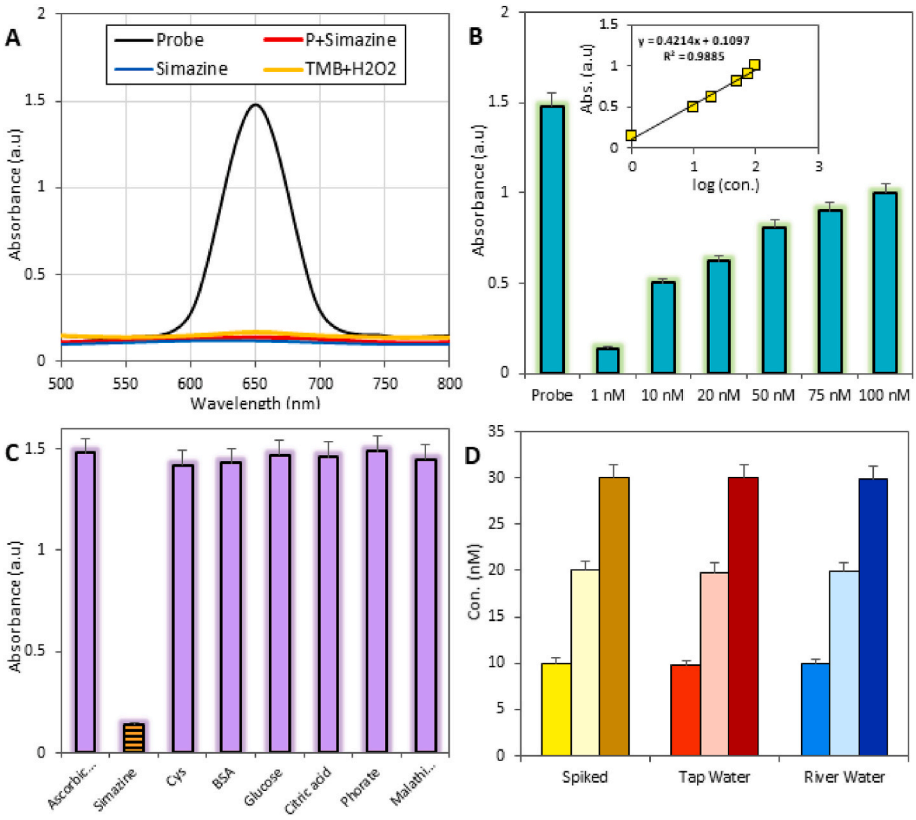

Fig. 9. (A) The UV–vis spectra for peroxidase colorimetric activity, (B) the effect of simazine concentration (inset: calibration curve), (C) the selectivity test, and (D) the simazine detection from tap and river waters.

products detected and are illustrated in Table S2. According to the LC-ESI-MS results, the degradation reaction was conducted by using the attack of $^1O_2$ on the e^-/rich groups. In the first stage, TC ($m/z = 445$) was attacked by $^1O_2$ and demethylation and dehydroxylation of the dimethylamino group and converted to form M1 ($m/z = 415$). Secondly, oxidative ring opening, and decarbonylation reactions were occurred to form M2 ($m/z = 318$) [60]. Then, M3 ($m/z = 274$) is produced by the dealkylation and oxidation reactions, and converting to M4 ($m/z = 218$) [60]. Finally, these intermediates can oxidized to smaller molecules of M5 ($m/z = 162$) and M6 ($m/z = 83$) and are mineralized to CO_2, and H_2O.

3.4. Antibacterial activity performance

The region surrounding the antibiotic disc, known as the zone of inhibition, is devoid of bacterial growth. The greater the zone of inhibition, the more attacking the bacterium and the lower zone of inhibition become the bacteria less sensitive and more resistant. Fig. 8 depicts the antibacterial ability of Hal/MoO_{3-x} nanocomposites versus *Listeria monocytogenes* and *Neisseria gonorrhoeae*. As can be seen that the concentration of nanomaterials was increased, the bactericidal was enhanced. At 10 mg/L concentration, zones of inhibition for *L. monocytogenes*, and *N. gonorrhoeae* were 8.23 and 5.12 mm, respectively. At 100 mg/L concentration, zones of inhibition for *L. monocytogenes*, and *N. gonorrhoeae* were 25.14 and 19.88 mm, respectively (Fig. 8). The antibacterial mechanisms were dependent to oxidative stress and metal ion release from the Hal/MoO_{3-x} nanocomposites. The cell walls of *N. gonorrhoeae* was thicker than *L. monocytogenes,* and the nanomaterials was lowly penetrated to *N. gonorrhoeae* bacterial, compared to gram positive bacterial (*L. monocytogenes*) [26].

3.5. Colorimetric detection of simazine

The catalytic activity of the Hal/MoO_{3-x} nanocomposites was studied by applying TMB and shown in Fig. 9A. As can be observed that there is no absorbance for the TMB + H_2O_2 system without catalyst. With adding Hal/MoO_{3-x}, the absorbance of the system depicts a very large increase, displaying the increased catalytic ability of Hal/MoO_{3-x}. Moreover, the simazine without catalyst exhibits no absorbance value. The interaction between the Hal/MoO_{3-x} and simazine was performed in the presence of H_2O_2 + TMB. The results depicted with interaction, the absorbance was decreased as compared to probe. To explore the peroxidase-like activity of the Hal/MoO_{3-x}, the effect of simazine concentration was investigated. Fig. 9B displays the absorption values of the sensing system was enhanced with simazine dose decreasing in the range of 100 nM–1 nM. The simazine response plot depicts linear over the range from 1 nM to 100 nM with a $R^2 = 0.9884$ (inset of Fig. 9B). The LOD is calculated to be ~2.45 nM [61]. To study the identity of the prepared platform, we then investigated the selectivity of the system was investigated for simazine in the presence of interfering substances. It could be observed that this probe depicts an obvious response for detection of simazine in the presence of other materials (Fig. 9C). The applicability of prepared probe versus simazine detection was studied in various environmental samples. The details spiked concentration (10, 20, and 30 nM) and found concentration of different environmental samples are illustrated in Fig. 9D. The recovery of simazine was observed in ranged from 98.00 % to 100 % in different environmental samples. Thus, our prepared Hal/MoO_{3-x} nanocomposite can be efficient way to the detection of simazine in real samples [62].

4. Conclusions

In summary, Hal/MoO_{3-x} nanocomposite were fabricated by hydrothermal and calcination methods. The excitonic energy transfer process

involved in the Hal/MoO_{3-x} photocatalytic system were investigated. The results of ESR tests, and quenching experiments indicated the generation of $^1O_2$. The phosphorescence tests displayed the high triplet exciton concentration facilitated the generation of $^1O_2$ via energy transfer processes. Hal/MoO_{3-x} exhibited good degradation activity in removal of TC. The rate constant of the Hal/MoO_{3-x} nanocomposites is 5.64 and 3.02 times higher than that of Hal, and MoO_{3-x}, respectively. LC-ESI-MS test results illustrate that the degradation process of TC is dominated by the selective attack of the $^1O_2$ on the electron-rich groups. Hal/MoO_{3-x} has the best antibacterial efficiently on the *L. monocytogenes*, and *N. gonorrhoeae*. Remarkably, the synthesized Hal/MoO_{3-x} nanocomposites shows high peroxidase-like activity could the oxidation of TMB by H_2O_2 to simazine detection in real samples. Finally, this work is promising way to the singlet oxygen activation, TC degradation, antibacterial agent, ad simazine detection.

CRediT authorship contribution statement

Khursheed Muzammil: Methodology; Investigation; Formal analysis; Resources.

Muhaned Zaid: Formal analysis; Methodology; Investigation; Validation.

Uday Abdul-Reda Hussein: Formal analysis; Methodology; Investigation; Validation.

Maryam Hazem Abduljabbar: Formal analysis; Methodology; Investigation; Validation.

Sarah Salah Jalal: Formal analysis; Methodology; Investigation; Software; Data curation.

Mazin A.A. Najm: Formal analysis; Methodology; Investigation; Software.

Mohammad Y. Alshahrani: Formal analysis; Methodology; Investigation: Resources.

Abbas F. Almulla: Formal analysis; Methodology; Investigation; Validation.

Ali Alsaalamy: Investigation; Validation; Software; Data curation; Software; Data curation.

Ramadan Fallah Amer: Methodology; Investigation; Formal analysis; Validation.

Baadal Jushi Janani: review & editing; Methodology; Investigation; Validation; Software Project administration; Conceptualization; Supervision.

Declaration of competing interest

The authors declare that they have no known competing financial interests or personal relationships that could have appeared to influence the work reported in this paper.

Data availability

No data was used for the research described in the article.

Acknowledgment

The authors extend their appreciation to the Deanship of Scientific Research at King Khalid University, KSA, for funding this work through a large research group program under grant number RGP.2/350/44.

Appendix A. Supplementary data

Supplementary data to this article can be found online at https://doi.org/10.1016/j.mssp.2023.107847.

References

[1] H. Yu, J. Zhu, R. Qiao, N. Zhao, M. Zhao, L. Kong, Facile preparation and controllable absorption of a composite based on PMo12/Ag nanoparticles: photodegradation activity and mechanism", ChemistrySelect 7 (2) (2022), e202103668 https://doi.org/10.1002/slct.202103668.

[2] Z. Dai, Z. Ma, X. Zhang, J. Chen, R. Ershadnia, X. Luan, M.R. Soltanian, An integrated experimental design framework for optimizing solute transport monitoring locations in heterogeneous sedimentary media, J. Hydrol. 614 (2022), 128541, https://doi.org/10.1016/j.jhydrol.2022.128541.

[3] X. Zhang, Z. Wang, P. Reimus, F. Ma, M.R. Soltanian, B. Xing, Z. Dai, Plutonium reactive transport in fractured granite: multi-species experiments and simulations, Water Res. 224 (2022), 119068, https://doi.org/10.1016/j.watres.2022.119068.

[4] Xiupeng Yue, Yongping Shan, Yaping Zhang, Role of direct current on thermal activated peroxydisulfate to degrade phenanthrene in soil: conversion of sulfate radical and hydroxyl radical to singlet oxygen, accelerated degradation rate and reduced efficiency, J. Hazard Mater. 452 (2023), 131187.

[5] Han Jia, Lei Wang, Xue-Bin Wang, Photogeneration of singlet oxygen catalyzed by hexafluoroisopropanol for selective degradation of dyes, iScience 26 (2023), 107306.

[6] Yu-Wei Li, Shu-Zhi Li, Wan-Li Ma, Acid-induced tubular g-C3N4 for the selective generation of singlet oxygen by energy transfer: implications for the photocatalytic degradation of parabens in real water environments, Sci. Total Environ. 896 (2023), 165316.

[7] Efraím A. Serna-Galvis, Yudy L. Martínez-Mena, Ricardo A. Torres-Palma, Zeolite 4A activates peroxymonosulfate toward the production of singlet oxygen for the selective degradation of organic pollutants, Chem. Eng. Res. Des. 193 (2023) 121–131.

[8] Jialing Sheng, Aimin Lu, Hongmei Jiang, Superior bensulfuron-methyl degradation performance of sphercial magnetic Co3O4@C-500/peroxymonosulfate system by enhancing singlet oxygen generation: the effect of oxygen vacancies, Chem. Eng. J. 471 (2023), 143945.

[9] Sihyeon Jo, Hyejin Kim, Jonghun Lim, Unraveling Janus-like behavior of copper phosphide for selective production of reactive oxygen species: singlet oxygen versus hydroxyl radical, Chem. Eng. J. 470 (2023), 144389.

[10] X. Feng, L. Sun, W. Wang, Y. Zhao, J. Shi, Construction of CdS@ZnO core–shell nanorod arrays by atomic layer deposition for efficient photoelectrochemical H2 evolution, Separ. Purif. Technol. 324 (2023), 124520, https://doi.org/10.1016/j.seppur.2023.124520.

[11] S. Wei, T. Chen, H. Hou, Y. Xu, Recent advances in electrochemical sterilization, J. Electroanal. Chem. 937 (2023), 117419, https://doi.org/10.1016/j.jelechem.2023.117419.

[12] Ying Chen, Jihad Ali, Baadal Jushi Janani, A facile preparation method for efficiency a novel LaNiO3/SrCeO3 (p-n type) heterojunction catalyst in photocatalytic activities, bactericidal assessment and dopamine detection, Surface. Interfac. 38 (2023), 102830.

[13] Asad Syed, Abdallah M. Elgorban, Baadal Jushi Janani, Highly-impressive performances of novel NiCo2O4/Bi2O3/Ag2ZrO3 nanocomposites in photocatalysis system, removal pathway, toxicity estimation, and antibacterial activities, J. Taiwan Inst. Chem. Eng. 149 (2023), 105004.

[14] X. Feng, B. Wang, G. Gao, S. Gao, C. Xie, J. Shi, MnyCo3−yOx bimetallic oxide prepared by ultrasonic technology for significantly improved catalytic performance in the reduction of NOx with NH3, Fuel 352 (2023), 129159, https://doi.org/10.1016/j.fuel.2023.129159.

[15] Y. Zheng, Y. Liu, X. Guo, Z. Chen, W. Zhang, Y. Wang, Y. Zhao, Sulfur-doped g-C3N4/rGO porous nanosheets for highly efficient photocatalytic degradation of refractory contaminants, J. Mater. Sci. Technol. 41 (2020) 117–126, https://doi.org/10.1016/j.jmst.2019.09.018.

[16] S. Pang, C. Zhou, Y. Sun, K. Zhang, W. Ye, X. Zhao, B. Hui, Natural wood-derived charcoal embedded with bimetallic iron/cobalt sites to promote ciprofloxacin degradation, J. Clean. Prod. 414 (2023), 137569, https://doi.org/10.1016/j.jclepro.2023.137569.

[17] R.S. Datta, F. Haque, M. Mohiuddin, B.J. Carey, N. Syed, A. Zavabeti, B. Zhang, H. Khan, K.J. Berean, J.Z. Ou, N. Mahmood, K. Kalantar-zadeh, Highly active two dimensional α-MoO3−x for the electrocatalytic hydrogen evolution reaction, J. Mater. Chem. A 5 (2017) 24223–24231.

[18] Masahito Morita, Satoshi Toyoda, Hisao Kiuchi, Takeshi Abe, Kazuhiro Kumagai, Takahiro Saida, Katsutoshi Fukuda, Chromogenic amorphous MoO_{3-x} nanosheets and their nanostructured films for smart window applications, ACS Appl. Nano Mater. 4 (9) (2021) 8781–8788.

[19] Ying Lai, Fakhri Ali, Baadal Jushi Janani, Synergistic activities of silver indium sulfide/nickel molybdenum sulfide nanostructures anchored on clay mineral for light-driven bactericidal performance, and detection of uric acid from gout patient serum, J. Photochem. Photobiol. B Biol. 234 (2022), 112526.

[20] M. Mylarappa, N. Raghavendra, K.N. Shravana Kumara, Study of ZnO nanoparticle supported clay minerals for electrochemical sensors, photocatalysis, and antioxidant applications, Chem. Phys. Mater. (2023), https://doi.org/10.1016/j.chphma.2023.07.002.

[21] Imane Daou, Gisèle Laure Lecomte-Nana, Nicolas Tessier-Doyen, Claire Peyratout, Maurice François Gonon, René Guinebretiere, Probing the dehydroxylation of kaolinite and halloysite by in situ high temperature X-ray diffraction, Minerals 10 (2020) 480, https://doi.org/10.3390/min10050480.

[22] Zikang Wang, Simin Yu, Jinling Diao, Effects of simazine herbicide on a plant-arthropod-lizard tritrophic community in territorial indoor microcosms: beyond the toxicity, Sci. Total Environ. 781 (2021), 146723.

[23] L.I.A.O. Min, X.I.E. Xiaomei, Effects of combination of plant and microorganism on degradation of simazine in soil, J. Environ. Sci. 20 (2008) 195–198.

[24] Shanna H. Swan, Robin L. Kruse, Liu Fan, Dana B. Barr, Erma Z. Drobnis, J Bruce Redmon, Christina Wang, Charlene Brazil, James W Overstreet, Semen quality in relation to biomarkers of pesticide exposure, Environ. Health Perspect. 111 (12) (2003) 1478–1484.

[25] B. Caffee, H. Wu, Factors affecting firefighter occupational cancer risk adjustment, Emerg. Manag. Sci. Technol. 2 (2022) 8, https://doi.org/10.48130/EMST-2022-0008, 2022.

[26] H. Mo, J. Shen, Y. Zhong, Z. Chen, T. Wu, Y. Lv, Y. Xie, Y. Hao, CircMAN1A2 promotes vasculogenic mimicry of nasopharyngeal carcinoma cells through upregulating ERBB2 via sponging miR-940, Oncol. Res. 31 (2022) 187–199, https://doi.org/10.32604/or.2022.027534, 2023.

[27] Ayat Ammar Mahdi, Ruaa Ali Obeid, Fakhri Ali, A facile construction of NiV2O6/CeO2 nano-heterojunction for photo-operated process in water remediation reaction, antibacterial studies, and detection of D-Amino acid in peroxidase system, Surface. Interfac. 40 (2023), 102970.

[28] Zhiming Liu, Mohammed Abdul Hadi, Fakhri Ali, High efficiency of Ag0 decorated Cu2MoO4 nanoparticles for heterogeneous photocatalytic activation, bactericidal system, and detection of glucose from blood sample, J. Photochem. Photobiol. B Biol. 236 (2022), 112571.

[29] Xixi Yao, Yamamah Jawad Bahr Aluloom, Fakhri Ali, Multipurpose properties the Z-scheme dimanganese copper oxide/cadmium sulfide nanocomposites for photo- or photoelectro-catalytic, antibacterial applications, and thiamine detection process, J. Photochem. Photobiol. Chem. 436 (2023), 114374.

[30] Shunhua Xiao, Fakhri Ali, Baadal Jushi Janani, Synthesis of spinel Tin ferrite decorated on Bismuth ferrite nanostructures for synergetic photocatalytic, superior drug delivery, and antibacterial efficiencies, Surface. Interfac. 27 (2021), 101490.

[31] Ashkan Bahadoran, Qinglei Liu, Vinod Kumar Gupta, Fabrication and structural of gold/cerium nanoparticles on tin disulfide nanostructures and decorated on hyperbranched polyethyleneimine for photocatalysis, reduction, hydrogen production and antifungal activities, J. Photochem. Photobiol. Chem. 416 (2021), 113316.

[32] Y. Dong, H. Yuan, D. Ge, N. Zhu, A novel conditioning approach for amelioration of sludge dewaterability using activated carbon strengthening electrochemical oxidation and realized mechanism, Water Res. 220 (2022), 118704, https://doi.org/10.1016/j.watres.2022.118704.

[33] J. Hu, L. Zhao, J. Luo, H. Gong, N. Zhu, A sustainable reuse strategy of converting waste activated sludge into biochar for contaminants removal from water: modifications, applications and perspectives, J. Hazard Mater. 438 (2022), 129437, https://doi.org/10.1016/j.jhazmat.2022.129437.

[34] Z. Xu, Y. Wang, S. Jiang, C. Fang, L. Liu, K. Wu, Y. Chen, Impact of input, preservation and dilution on organic matter enrichment in lacustrine rift basin: a case study of lacustrine shale in Dehui Depression of Songliao Basin, NE China, Mar. Petrol. Geol. 135 (2022), 105386, https://doi.org/10.1016/j.marpetgeo.2021.105386.

[35] R. Yang, E. Hou, W. Cheng, X. Yan, T. Zhang, S. Li, Y. Guo, Membrane-targeting neolignan-antimicrobial peptide mimic conjugates to combat methicillin-resistant Staphylococcus aureus (MRSA) infections, J. Med. Chem. 65 (24) (2022) 16879–16892, https://doi.org/10.1021/acs.jmedchem.2c01674, 2022.

[36] G. Zhang, Z. Zhao, X. Yin, Y. Zhu, Impacts of biochars on bacterial community shifts and biodegradation of antibiotics in an agricultural soil during short-term incubation, Sci. Total Environ. 771 (2021), 144751, https://doi.org/10.1016/j.scitotenv.2020.144751.

[37] Muhammad Aqeel Ashraf, Yafeng Yang, Fakhri Ali, Synthesis of NiS–MoO3 nanocomposites and decorated on graphene oxides for heterogeneous photocatalysis, antibacterial and antioxidant activities, Ceram. Int. 46 (2020) 8379–8384.

[38] Monmon Podder, Md Farid Ahmed, Nahid Sharmin, Effect of metal ions on structural, morphological and optical properties of nano-crystallite spinel cobalt-aluminate (CoAl2O4), Arab. J. Chem. 16 (2023), 104700.

[39] Y. Liu, L. Zong, C. Zhang, W. Liu, A. Fakhri, V.K. Gupta, Design and structural of Sm-doped SbFeO3 nanopowders and immobilized on poly (ethylene oxide) for efficient photocatalysis and hydrogen generation under visible light irradiation, Surface. Interfac. 26 (2021), 101292.

[40] A.K. Aldhalmi, S. Alkhayyat, W.K.Y. Albahadly, Jawad Ma, K.M. Alsaraf, A novel fabricate of iron and nickel-introduced bimetallic MOFs for quickly catalytic degradation via the peroxymonosulfate, antibacterial efficiency, and cytotoxicity assay, Inorg. Chem. Commun. 153 (2023), 110823.

[41] A. Bahadoran, Q. Liu, S. Masudy-Panah, J.R. De Lile, S. Ramakrishna, Assessment of silver doped cobalt titanate supported on chitosan-amylopectin nanocomposites in the photocatalysis performance under sunlight irradiation, and antimicrobial activity, Surface. Interfac. 25 (2021), 101191.

[42] A. Bahadoran, Q. Liu, B. Liu, J.J. Gu, D. Zhang, A. Fakhri, V.K. Gupta, Preparation of Sn/Fe nanoparticles for Cr (III) detection in presence of leucine, photocatalytic and antibacterial activities, Spectrochim. Acta Mol. Biomol. Spectrosc. 253 (2021), 119592.

[43] Cagil Zeynep, Sungu Akdogan, Burcu Gokcal, Mustafa Polat, Kadriye Ozlem Hamaloglu, Cigdem Kip, Tunce Ali, Porous, Oxygen vacancy enhanced CeO_{2-x} microspheres with efficient enzyme-mimetic and photothermal properties, ACS Sustainable Chem. Eng. 10 (29) (2022) 9492–9505.

[44] Y. He, L. Zhang, M.S. Tong, Microwave imaging of 3D dielectric-magnetic penetrable objects based on integral equation method, IEEE Trans. Antenn. Propag. 71 (2023) 5110–5120, https://doi.org/10.1109/TAP.2023.3262299, 2023.

[45] X. Wei, X. Bai, X. Wen, L. Liu, J. Xiong, C. Yang, A large and overlooked Cd source in karst areas: the migration and origin of Cd during soil formation and erosion, Sci. Total Environ. 895 (2023), 165126, https://doi.org/10.1016/j.scitotenv.2023.165126.

[46] Mehdi Chougan, Seyed Hamidreza Ghaffar, Mazen J. Al-Kheetan, Effect of natural and calcined halloysite clay minerals as low-cost additives on the performance of 3D-printed alkali-activated materials, Mater. Des. 223 (2022), 111183.

[47] Yu Ting, Baifa Zhang, Lala Setti Belaroui, Optimization of mechanical performance of limestone calcined clay cement: effects of calcination temperature of nanosized tubular halloysite, gypsum content, and water/binder ratio, Construct. Build. Mater. 389 (2023), 131709.

[48] Jian Qu, Xin Zhang, Jing Su, pH-controlled construction of 2D and 3D micro-nano hybrid carbon architectures with fluorescence/phosphorescence dual-mode emission for white-emitting diodes, Carbon 214 (2023), 118355.

[49] Piotr Bilski, Baozhong Zhao, Colin F. Chignell, Singlet oxygen phosphorescence photosensitized in nano-aggregates of C60 buckminsterfullerene is insensitive to solvent and quenchers and strongly red-shifted indicating highly polarizable interior, Chem. Phys. Lett. 458 (2008) 157–160.

[50] T.S.E. Ho-Yin, Chi Shun Yeung, Shao-Yuan Leu, One-pot synthesis to prepare lignin/photoacid nanohybrids for multifunctional biosensors and photo-triggered singlet oxygen generation, Green Chem. 24 (2022) 2904–2918.

[51] Wei Liu, Yingbo Dong, Hai Lin, Mechanism of aniline aerofloat and Cd^{2+} elimination from mining wastewater by customized S-scheme Halloysite@MoS_2/goethite nanotube: synergy of photo-Fenton decomplexation and adsorption, Appl. Surf. Sci. 626 (2023), 157307.

[52] X. Yi, H. Ji, C. Wang, Y. Li, Y. Li, C. Zhao, A. Wang, H. Fu, P. Wang, X. Zhao, W. Liu, Photocatalysis-activated SR-AOP over PDINH/MIL-88A(Fe) composites for boosted chloroquine phosphate degradation: performance, mechanism, pathway and DFT calculations, Appl. Catal. B Environ. 293 (2021), 120229.

[53] M. Hou, Y. Li, F. Peng, B. Daneshvar Rouyendegh, A new optimum technique for parameter identification of the proton exchange membrane fuel cells based on improved remora optimizer, Energy Sources, Part A Recovery, Util. Environ. Eff. 45 (1) (2023) 3019–3040, https://doi.org/10.1080/15567036.2023.2192011.

[54] Z. Zhang, M. Passlack, G. Pitner, C.H. Kuo, S.T. Ueda, J. Huang, P. Bandaru, Sub-nanometer interfacial oxides on highly oriented pyrolytic graphite and carbon nanotubes enabled by lateral oxide growth, ACS Appl. Mater. Interfaces 14 (9) (2022) 11873–11882, https://doi.org/10.1021/acsami.1c21743.

[55] Y. Zhang, H. Chung, J.P. Ngo, T. Monsoor, S.A. Hussain, J.H. Matsumoto, H. Nariai, Characterizing physiological high-frequency oscillations using deep learning, J. Neural. Eng. 19 (6) (2022), 066027, https://doi.org/10.1088/1741-2552/aca4fa.

[56] Junfeng Wen, Xia Liu, Vinod Kumar Gupta, Bimetal cobalt-Iron based organic frameworks with coordinated sites as synergistic catalyst for fenton catalysis study and antibacterial efficiency, Colloids Surf. A Physicochem. Eng. Asp. 610 (2021), 125683.

[57] H. Zhou, Y. Li, C. Yang, Y. Sun, Mixed-framework-based energy optimization of chemi-mechanical pulping, IEEE Trans. Ind. Inf. 16 (9) (2019) 5895–5904, https://doi.org/10.1109/TII.2019.2963347.

[58] X. Lin, K. Lu, A.K. Hardison, Z. Liu, X. Xu, D. Gao, W.S. Gardner, Membrane inlet mass spectrometry method (REOX/MIMS) to measure 15N-nitrate in isotope-enrichment experiments, Ecol. Indicat. 126 (2021), 107639, https://doi.org/10.1016/j.ecolind.2021.107639.

[59] Y. Liang, J. Li, Y. Xue, T. Tan, Z. Jiang, Y. He, Y. Pan, Benzene decomposition by non-thermal plasma: a detailed mechanism study by synchrotron radiation photoionization mass spectrometry and theoretical calculations, J. Hazard Mater. 420 (2021), 126584, https://doi.org/10.1016/j.jhazmat.2021.126584.

[60] Zhe Huang, Haicheng Liu, Insights into the pathways, intermediates, influence factors and toxicological properties in the degradation of tetracycline by TiO2-based photocatalysts, J. Environ. Chem. Eng. 11 (2023), 110587.

[61] Qiao-Fen Pan, Hai-Feng Jiao, Xi-Zhi Shi, Highly selective molecularly imprinted-electrochemiluminescence sensor based on perovskite/Ru(bpy)32+ for simazine detection in aquatic products, Sci. Total Environ. 843 (2022), 156925.

[62] Zipho Samuel, Mike O. Ojemaye, Anthony I. Okoh, Adsorption of simazine herbicide from aqueous solution by novel pyrene functionalized zinc oxide nanoparticles: kinetics and isotherm studies, Mater. Today Commun. 34 (2023), 105435.